



Electrochemical CH₄ oxidation into acids and ketones on ZrO₂:NiCo₂O₄ quasi-solid solution nanowire catalyst



Ming Ma^{a,*}, Cheoulwoo Oh^{b,1}, Jiwon Kim^{b,1}, Jun Hyuk Moon^c, Jong Hyeok Park^{b,*}

^a Shenzhen Key Laboratory of Nanobiomechanics, Shenzhen Institutes of Advanced Technology, Chinese Academy of Sciences, Shenzhen 518055, Guangdong, China

^b Department of Chemical and Biomolecular Engineering, Yonsei University, 50 Yonsei-ro, Seodaemun-gu, Seoul, 120-749, Republic of Korea

^c Department of Chemical and Biomolecular Engineering, Sogang University, 1 Sinsu-dong, Mapo-gu, Seoul, Republic of Korea

ARTICLE INFO

Keywords:
Electrocatalyst
Methane oxidation
Quasi-solid solution
Acid
Ketone

ABSTRACT

Efficient utilization of abundant methane (CH₄) from natural gas remains a major catalysis challenge. One recommended strategy is to convert methane into liquid fuels, such as alcohols, ketones and acids, but most processes usually proceed through high-temperature routes. Here, we employ a ZrO₂:NiCo₂O₄ quasi-solid solution catalyst as the electrochemical anode for partial methane oxidation. Without high temperature, noble metal catalysts and expensive oxidants, this quasi-solid solution anode produces propionic acid, acetic acid and acetone. After the analysis of the products, we demonstrate that the intermediate products from partial methane oxidation, 1-propanol, acetaldehyde and 2-propanol, are further oxidized into propionic acid, acetic acid and acetone, respectively. Long-term stable production via methane oxidation is a new strategy for the electrochemical conversion of organic chemicals.

1. Introduction

Methane (CH₄) is a major component of natural gas with lower carbon dioxide emissions when it is combusted. However, the emission of CH₄ cause the greenhouse effect with 30 times of CO₂ [1]. During the exploitation process of CH₄ from shale gas and marsh gas, the CH₄ emission would cause more serious environmental pollution and climate change. Thus, a suitable method to convert CH₄ to liquid fuels could solve aforementioned problems and, more importantly which will provide more value-added materials from CH₄. Numerous efforts have been made to directly convert CH₄ into liquid fuels, such as alcohols and ketones, as value-added materials [2–5]. Unfortunately, the proposed cyclic gas-phase conversion systems need high temperatures (> 200°) to activate CH₄ to produce CH₃OH due to the strength of the CH₃-H bond (435 kJ mol⁻¹) [6,7]. An alternative method, the liquid-phase conversion strategy, employs milder reaction conditions; however, high temperatures (180 °C) with strongly acidic media or highly oxidative and expensive hydrogen peroxide (H₂O₂) should be employed [8–11].

Electrochemical redox reactions have been employed to breakdown various stable chemicals, such as water (H₂O) and carbon dioxide (CO₂). [12–14] In particular, in the electrochemical reduction reaction of CO₂, various kinds of higher alcohol products can be obtained

depending on the catalyst used [15,16]. We have previously reported that electrochemical oxidation of CH₄ using a Co₃O₄/ZrO₂ mixture in an aqueous electrolyte at room temperature has been proven as an appropriate method with simple instruments to generate C1 to C3 liquid fuels [17]. However, the nonselective production of 1-propanol and 2-propanol makes it difficult to envisage a commercial-level process based on this method [17].

Applied with a relatively small bias, highly efficient and selective incorporation of CH₄ into higher alcohol products would represent substantial progress for more reliable and economically viable processes for a CH₄ conversion into value-added products. Thus, we designed a ZrO₂:NiCo₂O₄ quasi-solid solution nanowire catalyst with porous structure through a simple hydrothermal method to realize sufficient supplementation of the oxidizing agent source during the oxidation process. The fabrication process of the ZrO₂:NiCo₂O₄ quasi-solid solution nanowire catalyst and its function for CH₄ electrochemical oxidation are shown in Fig. 1. According to our experimental results, stable oxygenates, such as propionic acid, acetic acid and acetone, were produced, and the methane oxidation conversion efficiency achieved after 20 h was 47.5%.

* Corresponding authors.

E-mail addresses: ming.ma@siat.ac.cn (M. Ma), lutts@yonsei.ac.kr (J.H. Park).

¹ These authors contributed equally.

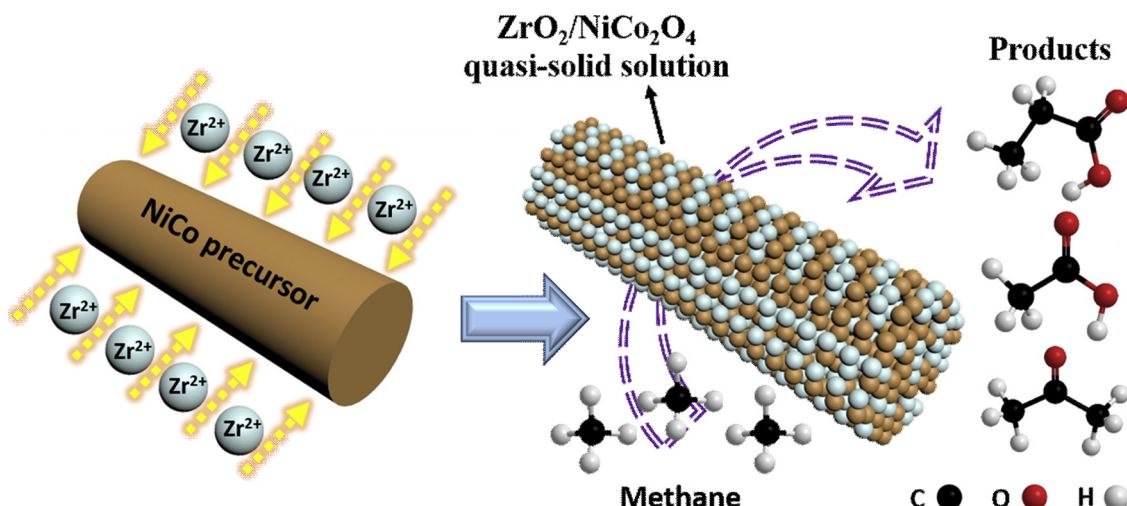


Fig. 1. The fabrication process of the $\text{ZrO}_2\text{:NiCo}_2\text{O}_4$ quasi-solid solution catalyst and its function for CH_4 electrochemical oxidation.

2. Experimental section

2.1. Electrocatalyst synthesis

All chemicals were used as received without further treatment. The $\text{ZrO}_2\text{:NiCo}_2\text{O}_4$ quasi-solid solution catalysts were synthesized using a hydrothermal method. For the 0.5- $\text{ZrO}_2\text{:NiCo}_2\text{O}_4$ sample, 0.322 g NiCl_2 (98%, Sigma Aldrich), 1.19 g $\text{CoCl}_2\text{-H}_2\text{O}$ ($\geq 98\%$, Sigma Aldrich), 0.117 g ZrCl_4 ($\geq 99.5\%$, Sigma Aldrich), 0.54 g urea (99.0–100.5%, Alfa Aesar), and 0.728 g hexadecyl trimethyl ammonium bromide ($\geq 99\%$, Acros Organics) were dissolved in 40 ml deionized (DI) water with vigorous stirring for 30 min, followed by sonication for 1 h to ensure homogeneous mixing. Then, the solution was transferred to a 60 ml autoclave container and heated at 120 °C for 48 h. After that, the powder was collected by centrifugation and washed with DI water 6 times to eliminate all residuals. Then, the precursor 0.5-Zr:NiCo was obtained. The 0.5- $\text{ZrO}_2\text{:NiCo}_2\text{O}_4$ sample was obtained after thermal annealing of the precursor at 500 °C for 3 h. To obtain the different ratios of the $\text{ZrO}_2\text{:NiCo}_2\text{O}_4$ samples, the amount of ZrCl_4 was changed to 0.047 g for 0.2- $\text{ZrO}_2\text{:NiCo}_2\text{O}_4$, 0.234 g for 1.0- $\text{ZrO}_2\text{:NiCo}_2\text{O}_4$, and 0.468 g for 2.0- $\text{ZrO}_2\text{:NiCo}_2\text{O}_4$ without changing the other conditions. For comparison, pure NiCo_2O_4 was prepared. Pure NiCo_2O_4 was synthesized by the same method used for the $\text{ZrO}_2\text{:NiCo}_2\text{O}_4$ synthesis without the addition of ZrCl_4 .

2.2. Electrocatalytic performance measurements

LSV measurements were conducted to compare the electrocatalytic performances of $\text{ZrO}_2\text{:NiCo}_2\text{O}_4$ and NiCo_2O_4 in a two-electrode system using a potentiostat (CH Instrument, CHI 660) with a glassy carbon electrode as the working electrode, Pt foil as the counter electrode and a 0.5 M Na_2CO_3 solution as the electrolyte. All working electrodes were prepared by dispersing powder samples in DI water at a concentration of 3 mg ml^{-1} and then dropping 20 μl of the dispersed solution on the surface of the glassy carbon electrode (area = 0.07 cm^2). After drying, a 5% Nafion 117 solution (Sigma Aldrich) was dropped on the surface of the electrode to cover the powder sample and form a surface film. Before each LSV measurement, the electrolyte was bubbled with Ar (99.9999%) or CH_4 (99.9999%) for 1 h to prepare the Ar- or CH_4 -saturated electrolyte.

2.3. Electrochemical CH_4 oxidation reaction

The electrochemical oxidation of CH_4 was conducted in a two-electrode system, employing graphite foil (Alfa) as the working

electrode, Pt foil as the counter electrode and 30 ml of a 0.5 M Na_2CO_3 solution as the electrolyte. The reactor was a closed cell with an approximately 395 ml gas-phase volume. The working electrode was prepared by dispersing the powder samples in DI water with a concentration of 3 mg ml^{-1} and then dropping 5.7 ml of the dispersed solution on the surface of the graphite foil (area = 20 cm^2). After drying, 1.5 ml of a 5% Nafion 117 solution was dropped to cover the sample on the graphite foil, followed by drying the sample at room temperature. Before the electrochemical reaction, the electrolyte was bubbled with CH_4 for 1 h to remove the oxygen and fill the space in the reaction instrument. After that, the instrument was quickly closed to prevent gas emission. Then, the electrochemical oxidation of CH_4 was conducted at 2.0 V vs. Pt for 5 h, 12 h and 20 h. The reaction temperature was controlled by water bath with room temperature, which was maintained at 25 °C.

2.4. Characterizations

The morphology analysis was carried out using field-emission scanning electron microscopy (FESEM, JEOL-7800 F) and transmission electron microscopy (TEM, JEM-F200). XRD patterns were measured using SmartLab in a Bragg-Brentano geometry. XPS data were obtained from a K-alpha instrument (Thermo Scientific Inc., UK). $^1\text{H-NMR}$ was conducted using an Advance III HD 400 400 MHz FT-NMR instrument (Bruker Biospin), and the samples were prepared by mixing 0.4 ml of the product solution with 0.2 ml D_2O . The amount of methane was determined using a 7890B GC instrument (Agilent Technologies).

3. Results and discussion

Noble metals have been extensively explored for methane conversion [18–20]. However, their high cost and scarcity restrict their applications in industrial manufacturing. Instead, transition metal oxides have received more attention due to their abundance and relatively high catalytic activity [21], which depends on their reducible properties. Reducible oxides are characterized by their oxygen exchange capability via a relatively easy route. The absence of oxygen, generally as an oxygen vacancy, results in excess electrons that are redistributed on empty cation levels, which give rise to high lattice oxygen mobility, resulting in catalytic oxidation activity [22,23]. Among these reducible oxides, cobalt oxide (Co_3O_4), a spinel oxide that consists of Co^{2+} at tetrahedral sites and Co^{3+} at octahedral sites in its lattice, has attracted much attention for methane oxidation applications. The relatively weak Co-O bonds allow easy production of oxygen vacancies under mild conditions, and the oxide is resistant to corrosion in alkaline media

[22–27]. Application of only 0.23 eV on the surface of Co_3O_4 can realize oxygen vacancy migration [28]. Comparing to Co_3O_4 , nickel cobalt oxide (NiCo_2O_4) has been demonstrated to perform higher catalytic activity for chemical redox reactions [29–31]. During the formation of NiCo_2O_4 , Ni cations are well integrated into the Co_3O_4 crystal lattice due to the high oxygen vacancy density on Co_3O_4 surface, and the atomic scale mixture with Ni cations [24,32] causes NiCo_2O_4 to have the same spinel structure as Co_3O_4 . DFT (density functional theory) calculations have been conducted to investigate the active sites of NiCo_2O_4 for the dissociation of the first C-H bond in the primary CH_4 oxidation process [27]. The calculation results suggest that Ni atoms on the surface of NiCo_2O_4 have a much lower activation barrier for dissociating CH_4 to CH_3 than the Co atoms, illustrating the Ni cations as active sites in NiCo_2O_4 for CH_4 electrochemical oxidation. After the first activation of CH_4 , the CH_3 species will couple with lattice oxygen atoms to form CH_3O species, which are important intermediates to produce liquid fuels. Moreover, the binding energy of CH_2 species on Ni cations is too low to realize further dehydrogenation of CH_3 , resulting in the formation of stable CH_3O species [27]. Because of the high activity and low cost of NiCo_2O_4 , $\text{ZrO}_2:\text{NiCo}_2\text{O}_4$ could be a very promising catalyst for electrochemical catalytic CH_4 oxidation due to the high catalytic activity from NiCo_2O_4 and good oxygen source delivery from ZrO_2 .

The $\text{ZrO}_2:\text{NiCo}_2\text{O}_4$ quasi-solid solution catalyst was synthesized by a hydrothermal method (details in the experimental section). The morphologies of the NiCo and Zr:NiCo precursors with different Zr

ratios can be observed from the SEM (scanning electron microscopy) images (Fig. 2 and S1). The precursors with different ratios are denoted as NiCo, 0.2-Zr:NiCo, 0.5-Zr:NiCo, 1.0-Zr:NiCo and 2.0-Zr:NiCo. The NiCo precursor (Fig. 2a) showed aggregated nanostructures consisting of short nanowires. Fig. S1 shows the structural variation that occurred with the addition of Zr atoms in the precursors, but the nanowire morphology remained. The length of the nanowires increased with the addition of Zr atoms. The 0.5-Zr:NiCo precursor (Fig. 2b) showed the most uniform morphology of the samples and a more elongated 1D morphology than the pure NiCo precursor; this sample also showed the best performance for CH_4 oxidation. However, with the increased Zr content in 1.0-Zr:NiCo and 2.0-Zr:NiCo, the nanowire diameters increased and additional small particles were present on the surface due to ZrO_2 crystals precipitating from the quasi-solid solution. After high-temperature annealing of the precursors, the final samples were obtained as NiCo_2O_4 and $\text{ZrO}_2:\text{NiCo}_2\text{O}_4$ with different Zr ratios, which were denoted as 0.2-Zr₂O₃:NiCo₂O₄, 0.5-Zr₂O₃:NiCo₂O₄, 1.0-Zr₂O₃:NiCo₂O₄ and 2.0-Zr₂O₃:NiCo₂O₄. Their morphologies were observed in SEM images, as shown in Figs. 2 and S2. During high-temperature annealing, the precursors changed to porous nanowires consisting of small nanoparticles. Pure NiCo_2O_4 (Fig. 2c) consisted of porous nanowires that were partially broken due to the aggregated state of the NiCo precursor. However, porous 0.5-Zr₂O₃:NiCo₂O₄ well maintained the nanowire structure and had a highly disperse nature, which contributed to its good catalytic ability. For the 1.0-Zr₂O₃:NiCo₂O₄ and

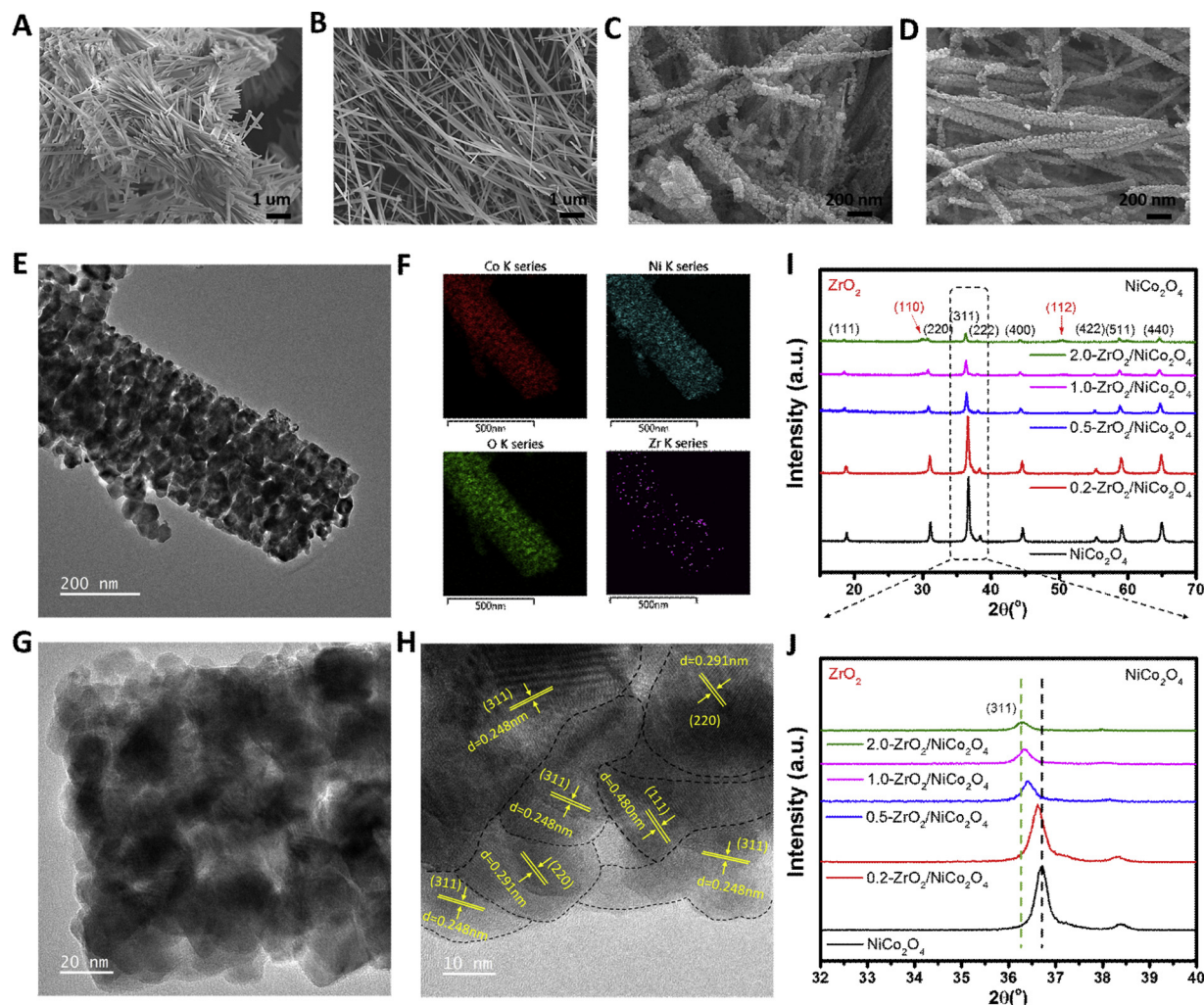


Fig. 2. SEM images of the (a) NiCo precursor, (b) 0.5-Zr:NiCo precursor, (c) NiCo_2O_4 and (d) 0.5-Zr₂O₃:NiCo₂O₄. (e) TEM image and (f) element mapping of 0.5-Zr₂O₃:NiCo₂O₄. (g, h) High-resolution TEM images of 0.5-Zr₂O₃:NiCo₂O₄. (i,j) XRD patterns of NiCo_2O_4 and $\text{ZrO}_2:\text{NiCo}_2\text{O}_4$ quasi-solid solution samples.

Table 1

BET analysis of synthesized of NiCo_2O_4 , 0.2-ZrO₂:NiCo₂O₄, 0.5-ZrO₂:NiCo₂O₄, 1.0-ZrO₂:NiCo₂O₄ and 2.0-ZrO₂:NiCo₂O₄.

Sample	NiCo_2O_4	0.2-ZrO ₂ :NiCo ₂ O ₄	0.5-ZrO ₂ :NiCo ₂ O ₄	1.0-ZrO ₂ :NiCo ₂ O ₄	2.0-ZrO ₂ :NiCo ₂ O ₄
Specific surface area (m^2/g)	11.065	14.939	13.574	18.375	28.319

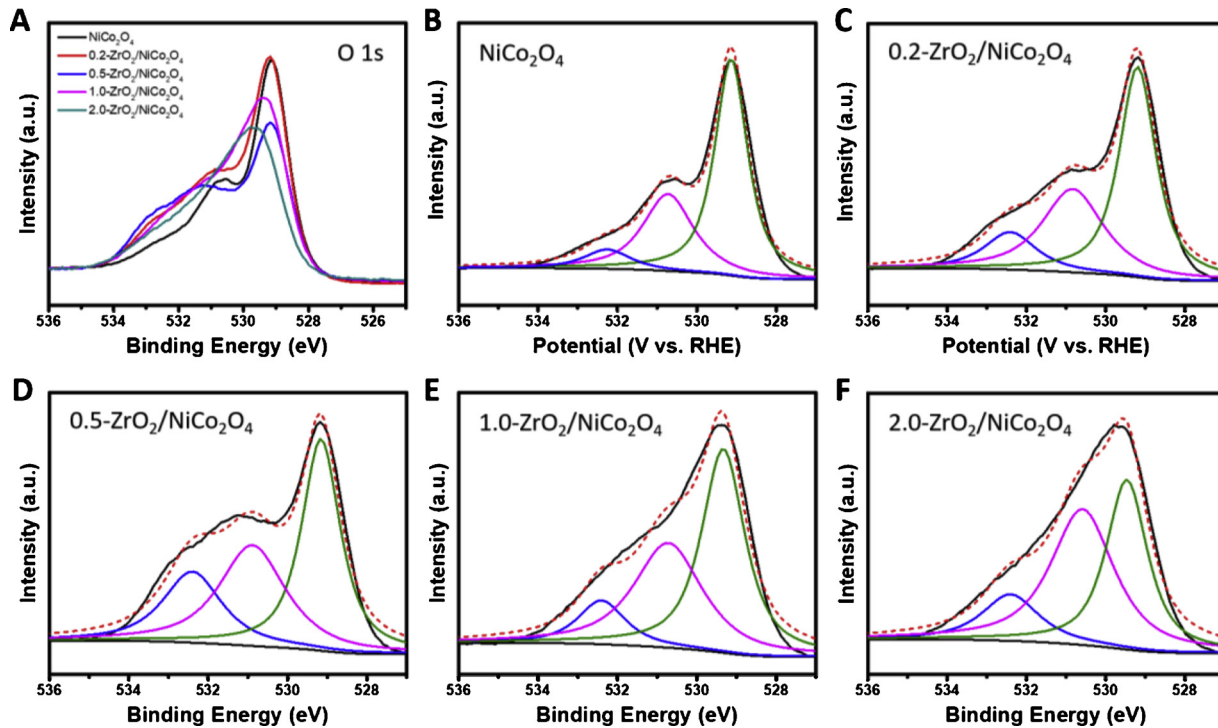


Fig. 3. (a) Overlapped and (b–f) deconvoluted O 1s XPS signals of NiCo_2O_4 and $\text{ZrO}_2:\text{NiCo}_2\text{O}_4$ quasi-solid solution samples.

2.0-ZrO₂:NiCo₂O₄ samples (Fig. S2), the nanoparticle size increased with large isolated particles, which were exsolute ZrO₂ particles. The destruction of the structure integrality by exsolute ZrO₂ may destroy the quasi-solid solution balance and thereby reduce the catalytic performance of ZrO₂:NiCo₂O₄ samples for CH₄ oxidation.

The nitrogen physisorption measurements (BET) have been conducted and shown in Table 1. From the BET analysis, ZrO₂:NiCo₂O₄ samples showed enlarged specific surface area when compared to the NiCo_2O_4 sample due to the addition of ZrO₂ component and the aggregative state of NiCo_2O_4 itself, which can be confirmed from Figs. S1 and S2. For the ZrO₂:NiCo₂O₄ samples, 1.0-ZrO₂:NiCo₂O₄ and 2.0-ZrO₂:NiCo₂O₄ show increased specific surface area according to the increase of ZrO₂ component amount. These two samples have relatively short nanorods structure and large diameter with additional ZrO₂ crystals precipitating from the quasi-solid solution, which should be responsible for the increased specific surface area. In addition, the 0.5-ZrO₂:NiCo₂O₄ sample shows relatively smallest specific surface area among the ZrO₂:NiCo₂O₄ samples, which should be ascribed to the well integration of ZrO₂ into NiCo_2O_4 to form the optimized quasi-solid solution. 0.5-ZrO₂:NiCo₂O₄ presents superior uniformity with long nanorods structure as shown in Figs. S1 and S2.

TEM (transmission electron microscopy) measurements were used to investigate the crystal structures of 0.5-ZrO₂:NiCo₂O₄, as shown in Fig. 2e. The 0.5-ZrO₂:NiCo₂O₄ nanowires has cross-connected uniform particles with a 20–50 nm size. The dissolution of ZrO₂ into the NiCo_2O_4 crystalline structure created homogeneous small particles, as shown in the TEM image, and this result is consistent with the element mapping results shown in Fig. 2f, demonstrating the quasi-solid solution state of 0.5-ZrO₂:NiCo₂O₄. From the high-resolution TEM (HR-TEM) images (Fig. 2g and h), the cross-connected structure of each

small particle can be clearly observed. The lattice constants of NiCo_2O_4 are 0.248 nm, 0.291 nm and 0.480 nm, corresponding to the (311), (220) and (111) facets, respectively. The particles with different facets are separated by dashed lines in the HR-TEM image. Meanwhile, the ZrO₂ crystal could not be found based on its lattice constant, indicating a solid solution of ZrO₂ and NiCo_2O_4 . However, in the transition area between each crystal particle, an amorphous phase could be observed, which is caused by the insertion of ZrO₂. Therefore, the results confirmed that 0.5-ZrO₂:NiCo₂O₄ has a quasi-solid solution structure. More evidence will be provided in the following section. In addition, the crystalline structures of the NiCo_2O_4 and ZrO₂:NiCo₂O₄ samples were analyzed by powder X-ray diffraction (XRD) using Cu K α radiation (Fig. 2i and j). The diffraction peaks of NiCo_2O_4 correspond to the cubic phase (JCPDS No. 20-0781), and the peaks of ZrO₂ correspond to the tetragonal phase (JCPDS No. 80-2155). In the XRD patterns, the typical (111), (220), (311), (222), (400), (422), (511) and (440) planes of NiCo_2O_4 were observed at approximately 18.9°, 31.1°, 36.7°, 38.3°, 44.6°, 55.4°, 59.1° and 65.0°, respectively; the typical (110) and (112) planes of ZrO₂ were observed at approximately 29.9° and 50.4°, respectively, in 1.0-ZrO₂:NiCo₂O₄ and 2.0-ZrO₂:NiCo₂O₄. The intensity of the typical NiCo_2O_4 peaks, especially the peak for the (311) facet, decreased with increasing Zr content. The insertion of ZrO₂ may lead to the crystal lattice of NiCo_2O_4 changing. In the magnified XRD patterns in Fig. 2f, the positions of the (311) peaks slightly shifted to the left with the increase in ZrO₂ content, which is similar to the change observed with Zr doping in other metal oxides [33,34], illustrating the homogeneous dispersion of Zr in the NiCo_2O_4 crystal. Based on the above discussion, ZrO₂:NiCo₂O₄ formed a quasi-solid solution structure, even after ZrO₂ crystals precipitated out of solution in the high Zr ratio samples.

To further investigate the chemical surface states of the samples, X-ray photoelectron spectroscopy (XPS) measurements were conducted. The XPS spectra of Ni 2p, Co 2p and Zr 3d are shown in Fig. S3. The binding energies of these three elements did not display obvious shifts with the changing Zr ratio. However, the intensities of the Ni and Co signals slightly decreased as the Zr ratio increased, and this decrease was partially due to the precipitated small ZrO_2 particles on the surface. Additionally, the O 1s signals of the NiCo_2O_4 and $\text{ZrO}_2:\text{NiCo}_2\text{O}_4$ samples were affected by the changing Zr ratio. The overlapping curves in Fig. 3a show that the O 1s signals of all $\text{ZrO}_2:\text{NiCo}_2\text{O}_4$ samples showed broader shoulders in the higher binding energy region, at approximately 532 eV, than the precursor, which indicates the presence of uncoordinated oxygen species. The presence of these species may be the reason for the enhanced CH_4 oxidation performance after the addition of ZrO_2 to NiCo_2O_4 . The O 1s signals can be clearly deconvoluted into three peaks at 529.2 eV, 530.8 eV and 532.4 eV (Fig. 3b–f). The peaks at 529.2 eV and 530.8 eV can be assigned to the oxygen in the oxide lattice and oxygen vacancies, respectively [35–37]. The peak at 532.4 eV is ascribed to uncoordinated oxygen species, such as chemisorbed or dissociated oxygen or hydroxyl species, which are defect sites [38,39]. Previous research has demonstrated that surface defect sites benefit electrolyte adsorption, which can improve liquid-phase electrocatalytic reactions [17,40]. Compared to pure NiCo_2O_4 , the $\text{ZrO}_2:\text{NiCo}_2\text{O}_4$ samples all had higher intensity O 1s XPS peaks at approximately 532.4 eV, illustrating the ability of ZrO_2 to improve surface charge adsorption. The 0.5- $\text{ZrO}_2:\text{NiCo}_2\text{O}_4$ sample had the largest ratio of these surface defect sites, resulting in the best CH_4 electrochemical oxidation performance. Additionally, with the increase in the Zr amount, the 1.0- $\text{ZrO}_2:\text{NiCo}_2\text{O}_4$ and 2.0- $\text{ZrO}_2:\text{NiCo}_2\text{O}_4$ samples showed slight increases in the intensity of the deconvoluted O 1s XPS peaks at approximately 530.8 eV, which are related to lattice oxygen vacancies, and a decrease in the intensity of the crystal oxygen peaks at approximately 529.2 eV. These changes may indicate the $\text{ZrO}_2:\text{NiCo}_2\text{O}_4$ crystal state is affected and result in the slightly lower CH_4 oxidation performance of 1.0- $\text{ZrO}_2:\text{NiCo}_2\text{O}_4$ and 2.0- $\text{ZrO}_2:\text{NiCo}_2\text{O}_4$.

The working electrodes were prepared by loading the NiCo_2O_4 or $\text{ZrO}_2:\text{NiCo}_2\text{O}_4$ samples on glassy carbon discs. The preparation details are provided in the experimental section. To investigate the electrochemical CH_4 oxidation performance, a two-electrode system was employed with the working electrode as the anode, Pt foil as the cathode and a sodium carbonate solution as the electrolyte. Fig. 4a shows the linear sweep voltammetry (LSV) curves of the NiCo_2O_4 and $\text{ZrO}_2:\text{NiCo}_2\text{O}_4$ samples in CH_4 -saturated electrolyte. All the ZrO_2 samples showed a higher current density than the pure NiCo_2O_4 sample. The 0.5- $\text{ZrO}_2:\text{NiCo}_2\text{O}_4$ sample showed the best performance for CH_4 oxidation, not only at the onset position but also at the overall current density. In addition, the LSV curves can be divided into two steps due to the different oxidation potentials of CH_4 and water. For all the $\text{ZrO}_2:\text{NiCo}_2\text{O}_4$ samples, the onset potential was observed at approximately 1.0 V vs. Pt, while the onset potential was approximately 1.5 V for the pure NiCo_2O_4 sample. The current density gradually increased up to ~2.0 V and then abruptly increased due to water oxidation. The 1.0- $\text{ZrO}_2:\text{NiCo}_2\text{O}_4$ and 2.0- $\text{ZrO}_2:\text{NiCo}_2\text{O}_4$ samples showed slightly poorer performance than 0.5- $\text{ZrO}_2:\text{NiCo}_2\text{O}_4$, which is likely due to the higher ZrO_2 amount. Even though the main function of ZrO_2 is to enhance the surface adsorption of carbonate ions, excess ZrO_2 precipitated on the surface in the higher ZrO_2 content samples and will affect charge transport during electrochemical oxidation at the ZrO_2 and NiCo_2O_4 interfaces, influencing the CH_4 oxidation performance. The LSV curves of the 0.5- $\text{ZrO}_2:\text{NiCo}_2\text{O}_4$ sample measured in Ar- and CH_4 -saturated electrolytes are provided in Fig. 4b. The 0.5- $\text{ZrO}_2:\text{NiCo}_2\text{O}_4$ sample showed an obviously enhanced current density in the CH_4 -saturated electrolyte compared to that observed in the Ar-saturated electrolyte, demonstrating its outstanding oxidation ability for CH_4 gas. Conversely, pure NiCo_2O_4 did not show a better electrocatalytic ability for CH_4 oxidation than water oxidation (Fig. S4), illustrating the individual

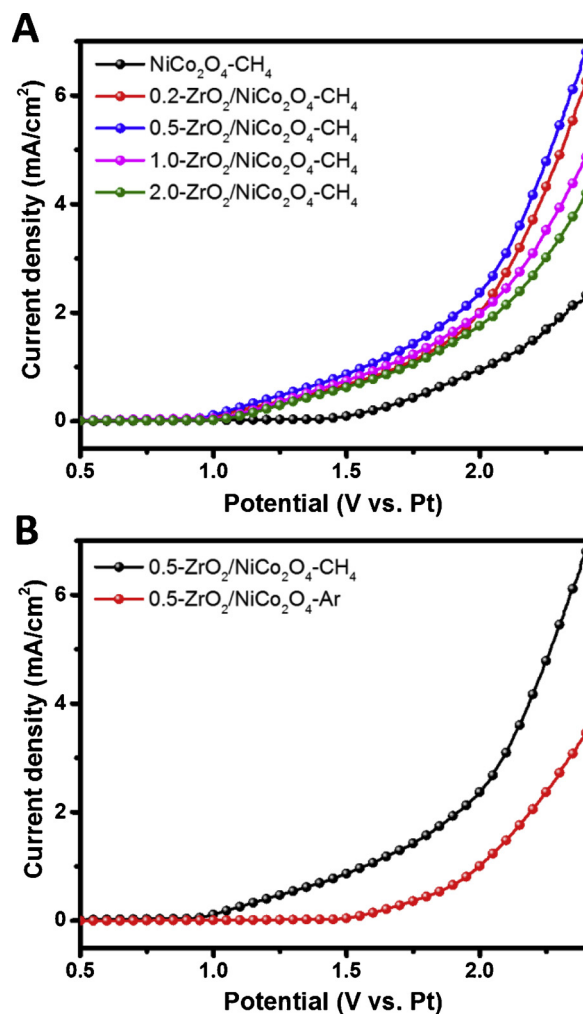


Fig. 4. (a) LSV curves of NiCo_2O_4 and $\text{ZrO}_2:\text{NiCo}_2\text{O}_4$ quasi-solid-solution samples for CH_4 electrochemical oxidation. (b) LSV curves of 0.5- $\text{ZrO}_2:\text{NiCo}_2\text{O}_4$ for CH_4 and water electrochemical oxidation.

functions of ZrO_2 and NiCo_2O_4 in the quasi-solid solution. ZrO_2 improves carbonate ion adsorption, and NiCo_2O_4 activates CH_4 under a bias. In addition, when comparing the J-V (current-voltage) curves of $\text{ZrO}_2:\text{NiCo}_2\text{O}_4$ with those of conventional $\text{ZrO}_2:\text{Co}_3\text{O}_4$ and $\text{ZrO}_2:\text{NiO}$ samples, the superior CH_4 oxidation ability of $\text{ZrO}_2:\text{NiCo}_2\text{O}_4$ is confirmed [17].

To measure the products from CH_4 oxidation, a two-electrode system was employed with catalyst-loaded carbon paper as the anode, Pt foil as the cathode and a carbonate solution as the electrolyte. The preparation and measurement details can be found in the experimental section. An electrochemical reactor under fully sealed conditions was employed, and the best catalyst (0.5- $\text{ZrO}_2:\text{NiCo}_2\text{O}_4$) was selected for the experiment. A 2.0 V bias was selected as the supplementary power for the CH_4 electrochemical conversion and was applied with vigorous stirring. After 5 h, 12 h and 20 h, the reaction was stopped, and the products were collected separately. ¹H-NMR (proton nuclear magnetic resonance) spectra were obtained to identify the products from the 0.5- $\text{ZrO}_2:\text{NiCo}_2\text{O}_4$ catalyst after different reaction times. The ¹H-NMR spectra for all reaction times are shown in Fig. 5a with the different products labelled. The ¹H-NMR spectrum of the electrolyte, a sodium carbonate solution, is provided in Fig. S5 for reference. The reaction process can be analyzed over the reaction time. First, after 5 h of reacting, the main products were 1-propanol and 2-propanol with small quantities of propionic acid and acetone and negligible acetic acid [41,42]. This result was in agreement with our previous work using

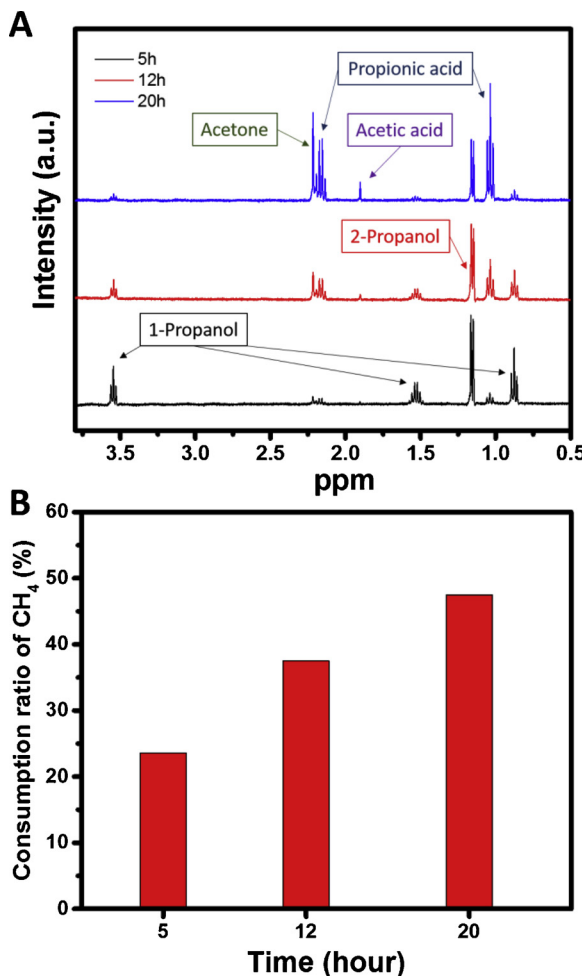


Fig. 5. (a) ^1H -NMR spectra of the products after 5 h, 12 h and 20 h of CH_4 electrochemical oxidation by 0.5-ZrO₂:NiCo₂O₄. (b) The consumption ratio of CH_4 after 5 h, 12 h and 20 h of the electrochemical reaction.

ZrO₂:Co₃O₄ as the catalyst for CH_4 oxidation [17]. Then, after 12 h of reacting, the intensity of the peaks related to 1-propanol and 2-propanol decreased, and the intensity of the propionic acid and acetone peaks increased, with some acetic acid appearing at 1.9 ppm. Finally, after 20 h of reacting, the peaks related to 1-propanol and 2-propanol further weakened, and those of 1-propanol almost disappeared. The intensity of the peaks belonging to propionic acid, acetone and acetic acid greatly increased, indicating they are the terminal products of the reaction. Compared with the products observed in the ^1H -NMR spectra, the quantities of other by-products were negligible.

To confirm the amount of CH_4 used in the reaction, GC (gas chromatography) was employed. The amounts of CH_4 consumed after reacting for 5 h, 12 h and 20 h are shown in Fig. 5b. The reference line of the CH_4 amount collected by GC measurements is shown in Fig. S6. After 20 h of reacting, 47.5% of the CH_4 gas in the sealed reactor was oxidized. In other words, the methane oxidation conversion efficiency after 20 h is 47.5%. In our previous report, acetaldehyde was the intermediate product during the CH_4 oxidation process [17]. However, in this process, 1-propanol and 2-propanol are the main primary products during the first 5 h of the reaction time, showing improved conversion efficiency due to the newly designed 0.5-ZrO₂:NiCo₂O₄ catalyst. Acetic acid containing two carbon atoms was one of the terminal products after 20 h, which can be converted from acetaldehyde without further addition reactions. Moreover, the rate of propionic acid and acetone production was further increased by extending the reaction time up to 20 h, and these are the product species directly converted from 1-

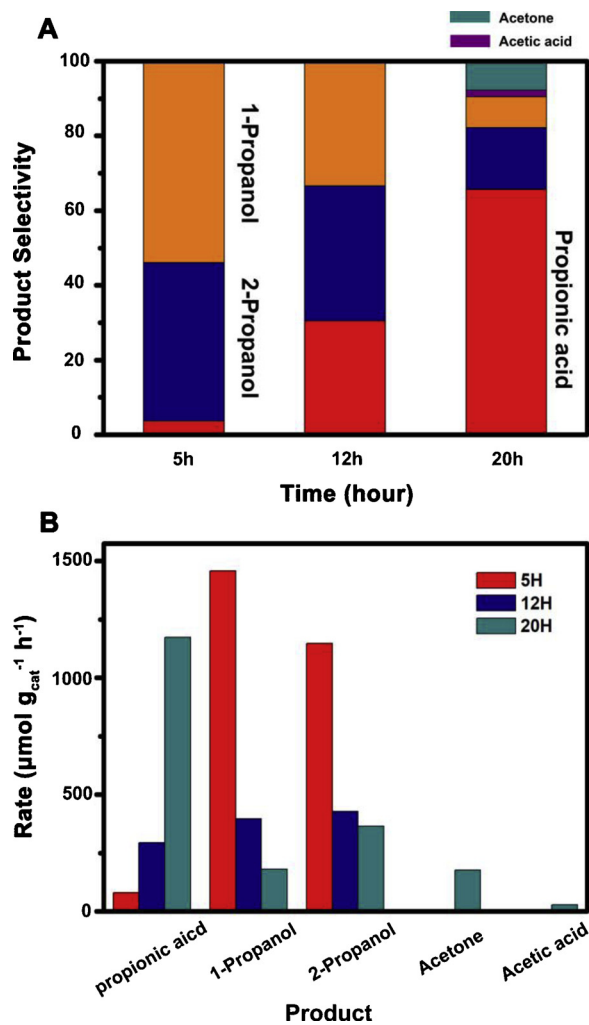


Fig. 6. (a) Product selectivity after 5 h, 12 h and 20 h of CH_4 electrochemical oxidation by 0.5-ZrO₂:NiCo₂O₄. (b) Production rate of propionic acid, 1-propanol, 2-propanol, acetone and acetic acid after 5 h, 12 h and 20 h.

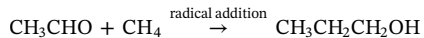
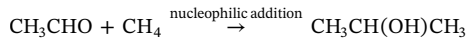
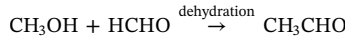
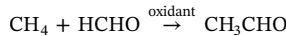
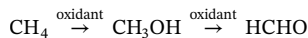
propanol and 2-propanol, respectively. 1-Propanol was almost completely consumed to form propionic acid after 20 h, which is due to the activity of 1-propanol that resulted from the radical addition process. The product selectivity with reaction time is shown in Fig. 6a, and the rate for the final main product (propionic acid) was calculated to be $1173 \mu\text{mol gcat}^{-1} \text{h}^{-1}$ (Fig. 6b) with approximately 65% selectivity among the products, i.e., 1-propanol, 2-propanol, acetic acid, acetone and propionic acid. Reference lines were prepared from the ^1H -NMR spectra of standard chemicals, as shown in Fig. S7, to calculate the production rate. In order to reveal the specialty of our work, comparisons with different oxidation methods using various metal oxide catalysts has been made in terms of the product types and conversion efficiencies as shown in Table 2. In addition, products of CH_4 electrochemical oxidation by 0.2-ZrO₂:NiCo₂O₄, 1.0-ZrO₂:NiCo₂O₄ and 2.0-ZrO₂:NiCo₂O₄ samples were measured as shown in Fig. S8. The production amounts by these three samples are much less than those by 0.5-ZrO₂:NiCo₂O₄. But for the propionic acid, acetone and acetic acid, the production amounts were increased as a function of reaction time, illustrating that the terminal product are those three species. For the 2.0-ZrO₂:NiCo₂O₄ sample, very few products can be obtained even with 20 h reaction, which may due to the decreased catalytic activity caused by the excess ZrO₂ component.

Based on our previous report, the reaction route to produce 1-propanol and 2-propanol can be summarized as shown below [17,55,56]

Table 2

Comparison of methane oxidation catalysts with different oxidation methods.

No.	Method	Catalysts	Products (production rate, $\mu\text{mol/g}_{\text{cat}}/\text{h}$)	CH ₄ conversion (%)	Ref.
1	H ₂ O ₂ assisted oxidation	Fe-silicalite-1	CH ₃ OH HCOOH CH ₃ OOH	10.5	[43]
2	K ₂ S ₂ O ₈ assisted oxidation	Fe-silicalite-1 and Cu/silicalite-1	CH ₃ OH	10.1	[44]
3	gaseous sulfur assisted oxidation	Au/SiO ₂	CH ₃ OH	24.9	[45]
4	thermal oxidation with O ₂	Pd/ZrO ₂	C ₂ H ₄	16.1	[46]
5	thermal oxidation with O ₂	Ni/CeO ₂	CO	98	[46]
		Li-MgO	CO C ₂ H ₄ C ₂ H ₆	38	[47]
6	thermal oxidation with O ₂	Na-W-Mn-SiO ₂	CO C ₂ H ₄ C ₂ H ₆	32.7	[48]
7	CO involved oxidation	Rh-ZSM-5	CH ₃ OH (1224) HCOOH (7753) CH ₃ COOH (4957)	—	[49]
8	photocatalytic oxidation	Cu-0.5/PCN	CH ₃ OH (24.5) CH ₃ CH ₂ OH (106)	—	[50]
9	photocatalytic oxidation	Pt/TiO ₂	C ₂ H ₆	1.1	[51]
10	photocatalytic oxidation	WO ₃	C ₂ H ₆ (2.9)	—	[52]
11	photocatalytic oxidation	WO ₃ /La	CH ₃ OH (27.1) C ₂ H ₆ (1.0)	—	[53]
12	photocatalytic oxidation	Zn-HPW/TiO ₂	CH ₃ OH (9.3)	—	[54]
13	electrochemical oxidation	ZrO ₂ /Co ₃ O ₄	CO (429) CH ₃ CHO CH ₃ CH ₂ CH ₂ OH CH ₃ CH(OH)CH ₃	40	[17]
14	electrochemical oxidation	ZrO ₂ :NiCo ₂ O ₄	CH ₃ CH ₂ CH ₂ OH (180) CH ₃ CH(OH)CH ₃ (363) CH ₃ CH ₂ COOH (1173) CH ₃ COCH ₃ (176) CH ₃ COOH (27)	47.5	This work



Acetaldehyde is the first key product, which can be obtained by reacting CH₄, methanol and formaldehyde via several reaction pathways. Methanol and formaldehyde are also formed from CH₄ oxidation. Then, 1-propanol and 2-propanol are produced through radical addition and nucleophilic addition reactions, respectively. Even with the enhanced catalyst in this work, the electrolyte with a carbonate oxidation source delivered by ZrO₂ was not changed. The mechanism in this work for producing 1-propanol and 2-propanol remained the same. According to the ¹H-NMR results, as the reaction time increased, the amounts of 1-propanol and 2-propanol both decreased due to their conversions to propionic acid and acetone. However, the rate of decrease in 1-propanol was higher than that of 2-propanol due to the higher thermodynamic stability of 2-propanol compared with that of 1-propanol. In addition, acetaldehyde, an intermediate product, is further oxidized into acetic acid after a long reaction time. The amount of acetaldehyde was insignificant because of its rapid consumption to form three-carbon-chain products. The formation mechanisms of propionic acid, acetone and acetic acid were almost the same as those for the electrochemical oxidation reactions of 1-propanol, 2-propanol and acetaldehyde, respectively. The reaction kinetics among these electrochemical oxidation reactions were different. Acetaldehyde was prior to producing propanol due to the mild oxidation conditions in our

electrochemical system. Thus, the amount of acetic acid converted from acetaldehyde was lower. Therefore, propionic acid and acetone became the main stable terminal products.

4. Conclusions

We found that the ZrO₂:NiCo₂O₄ quasi-solid solution catalyst is an efficient electrocatalyst for CH₄ oxidation with a carbonate solution as the electrolyte under an ambient environment. The ZrO₂:NiCo₂O₄ quasi-solid solution anode can activate CH₄ molecules with the application of small biases. The high reaction rate benefited from the high electrocatalytic activity of NiCo₂O₄. After a long reaction time, the first intermediate, 1-propanol, was almost completely oxidized into propionic acid, and the second intermediate, 2-propanol, was converted to acetone to some extent. This new solid-solution electrocatalyst with carbonate ion adsorption and efficient CH₄ activation could increase the speed of the CH₄ to higher alcohol conversion reaction. Three-carbon-chain ketones and acids were found to be the stable and final products.

Declaration of Competing Interest

The authors declare that they have no known competing financial interests or personal relationships that could have appeared to influence the work reported in this paper.

Acknowledgments

M. Ma, C. Oh and J. Kim contributed equally as co-first authors. This work was partially supported by the NRF of Korea Grant funded by the Ministry of Science, ICT and Future Planning (2019R1A2C3010479, 2019M3E6A1064525 <GN1>, <GN1> 2016M3D3A1A01913254 (C1 Gas Refinery Program)), and SIAT Innovation Program for Excellent

Young Researchers (201807).

References

- [1] D.T. Shindell, G. Faluvegi, D.M. Koch, G.A. Schmidt, N. Unger, S.E. Bauer, Improved attribution of climate forcing to emissions, *Science* 326 (2009) 716–718, <https://doi.org/10.1126/science.1174760>.
- [2] V.C.-C. Wang, S. Maji, P.P.-Y. Chen, H.K. Lee, S.S.-F. Yu, S.I. Chan, Alkane oxidation: methane monooxygenases, related enzymes, and their biomimetics, *Chem. Rev.* 117 (2017) 8574–8621, <https://doi.org/10.1021/acs.chemrev.6b00624>.
- [3] L. Nazaries, J.C. Murrell, P. Millard, L. Baggs, B.K. Singh, Methane, microbes and models: fundamental understanding of the soil methane cycle for future predictions, *Environ. Microbiol.* 15 (2013) 2395–2417, <https://doi.org/10.1111/1462-2920.12149>.
- [4] B.L. Conley, W.J. Tenn III, K.J.H. Young, S.K. Ganesh, S.K. Meier, V.R. Ziatdinov, O. Mironov, J. Osgaard, J. Gonzales, W.A. Goddard III, R.A. Periana, Design and study of homogeneous catalysts for the selective, low temperature oxidation of hydrocarbons, *Mol. Catal. A-Chem.* 251 (2006) 8, <https://doi.org/10.1016/j.molcata.2006.02.035>.
- [5] H.D. Gesser, N.R. Hunter, C.B. Prakash, The direct conversion of methane to methanol by controlled oxidation, *Chem. Rev.* 85 (1985) 235–244, <https://doi.org/10.1021/cr00068a001>.
- [6] E.V. Starokon, M.V. Parfenov, S.S. Arzumanov, L.V. Pirutko, A.G. Stepanov, G.I. Panov, Oxidation of methane to methanol on the surface of FeZSM-5 zeolite, *J. Catal.* 300 (2013) 47–54, <https://doi.org/10.1016/j.jcat.2012.12.030>.
- [7] L. Sushkevich, D. Palagin, M. Ranocchiai, J.A. van Bokhoven, Selective anaerobic oxidation of methane enables direct synthesis of methanol, *Science* 356 (2017) 523–527, <https://doi.org/10.1126/science.aam9035>.
- [8] R.A. Periana, D.J. Taube, E.R. Evitt, D.G. Loffler, P.R. Wentreck, G. Voss, T.A. Masuda, A mercury-catalyzed, high-yield system for the oxidation of methane to methanol, *Science* 259 (1993) 340–343, <https://doi.org/10.1126/science.259.5093.340>.
- [9] R.A. Periana, D.J. Taube, S. Gamble, H. Taube, T. Saton, H. Fujii, Platinum catalysts for the high-yield oxidation of methane to methanol derivative, *Science* 280 (1998) 560–564, <https://doi.org/10.1126/science.280.5363.560>.
- [10] R. Palkovits, M. Antonietti, P. Kuhn, A. Thomas, F. Schuth, Solid catalysts for the selective low-temperature oxidation of methane to methanol, *Angew. Chem. Int. Ed.* 48 (2009) 6909–6912, <https://doi.org/10.1002/anie.200902009>.
- [11] N. Agarwal, S.J. Freakley, R.U. McVicker, S.M. Althahban, N. Dimitratos, Q. He, D.J. Morgan, R.L. Jenkins, D.J. Willock, S.H. Taylor, C.J. Kiely, G.J. Hutchings, Aqueous Au-Pd colloids catalyze selective CH₄ oxidation to CH₃OH with O₂ under mild conditions, *Science* 358 (2017) 223–227, <https://doi.org/10.1126/science.aan6515>.
- [12] X. Shi, S. Siahrostami, G. Li, Y. Zhang, P. Chakrhanont, F. Studt, T.F. Jaramillo, X. Zheng, J.K. Norskov, Understanding activity trends in electrochemical water oxidation to form hydrogen peroxide, *Nat. Commun.* 8 (2017) 701, <https://doi.org/10.1038/s41467-017-00585-6>.
- [13] H. Malerod-Fjeld, D. Clark, I. Yuste-Tirados, R. Zanon, D. Catalan-Martinez, D. Beeaff, S.H. Morejudo, P.K. Vestre, T. Norby, R. Haugsrud, J.M. Serra, C. Kjolseth, Thermo-electrochemical production of compressed hydrogen from methane with near-zero energy loss, *Nat. Energy* 2 (2017) 923–931, <https://doi.org/10.1038/s41560-017-0029-4>.
- [14] R.G. Mariano, K. McKelvey, H.S. White, M.W. Kanan, Selective increase in CO₂ electroreduction activity at grain-boundary surface terminations, *Science* 358 (2017) 1187–1192, <https://doi.org/10.1126/science.aoa3691>.
- [15] Y. Jiao, Y. Zheng, P. Chen, M. Jaroniec, S.Z. Qiao, Molecular scaffolding strategy with synergistic active centers to facilitate electrocatalytic CO₂ reduction to hydrocarbon/alcohol, *J. Am. Chem. Soc.* 139 (2017) 18093–18100, <https://doi.org/10.1021/jacs.7b10817>.
- [16] E.L. Clark, C. Hahn, T.F. Jaramillo, A.T. Bell, Electrochemical CO₂ reduction over compressively strained CuAg surface alloys with enhanced multi-carbon oxygenate selectivity, *J. Am. Chem. Soc.* 139 (2017) 15848–15857, <https://doi.org/10.1021/jacs.7b08607>.
- [17] M. Ma, B.J. Jin, P. Li, M.S. Jung, J.I. Kim, Y. Cho, S. Kim, J.H. Moon, J.H. Park, Ultrahigh electrocatalytic conversion of methane at room temperature, *Adv. Sci.* 4 (2017) 1700379, , <https://doi.org/10.1002/advs.201700379>.
- [18] Z. Liang, T. Li, M. Kim, A. Asthagiri, J.F. Weaver, Low-temperature activation of methane on the IrO₂(110) surface, *Science* 356 (2017) 299–303, <https://doi.org/10.1126/science.aam9147>.
- [19] R. Horn, K.A. Williams, N.J. Degenstein, A. Bitsch-Larsen, D.D. Nogare, S.A. Tupy, L.D. Schmidt, Methane catalytic partial oxidation on autothermal Rh and Pt foam catalysts: oxidation and reforming zones, transport effects, and approach to thermodynamic equilibrium, *J. Catal.* 249 (2007) 380–393, <https://doi.org/10.1016/j.jcat.2007.05.011>.
- [20] Y. Chin, C. Buda, M. Neurock, E. Iglesia, Consequences of metal-oxide interconversion for C-H bond activation during CH₄ reactions on Pd catalysts, *J. Am. Chem. Soc.* 135 (2013) 15425–15442, <https://doi.org/10.1021/ja405004m>.
- [21] J. Li, X. Liang, S. Xu, J. Hao, Catalytic performance of manganese cobalt oxides on methane combustion at low temperature, *Appl. Catal. B-Environ.* 90 (2009) 307–312, <https://doi.org/10.1016/j.apcatb.2009.03.027>.
- [22] A.R. Puigdollers, P. Schlexer, S. Tosoni, G. Pacchioni, Increasing oxide reducibility: the role of metal/oxide interfaces in the formation of oxygen vacancies, *ACS Catal.* 7 (2017) 6493–6513, <https://doi.org/10.1021/acscatal.7b01913>.
- [23] X. Shi, S.L. Bernasek, A. Selloni, Formation, electronic structure, and defects of Ni substituted spinel cobalt oxide: a DFT + U study, *J. Phys. Chem. C* 120 (2016) 14892–14898, <https://doi.org/10.1021/acs.jpcc.6b03096>.
- [24] S. Zhang, J. Shan, Y. Zhu, A.I. Frenkel, A. Patlolla, W. Huang, S.J. Yoon, L. Wang, H. Yoshida, S. Takeda, F. Tao, WGS catalysis and in situ studies of CoO_{1-x}, PtCo_x/Co₃O₄, and Pt_nCo_m/CoO_{1-x} nanorod catalysts, *J. Am. Chem. Soc.* 135 (2013) 8283–8293, <https://doi.org/10.1021/ja401967y>.
- [25] V.E. Henrich, P.A. Cox, *The Surface Chemistry of Metal Oxides*, Cambridge Univ Press, 1994.
- [26] X.W. Xie, Y. Li, Z.Q. Liu, M. Haruta, W.J. Shen, Low-temperature oxidation of CO catalysed by Co₃O₄ nanorods, *Nature* 458 (2009) 746–749, <https://doi.org/10.1038/nature07877>.
- [27] F.F. Tao, J.J. Shan, L. Nguyen, Z. Wang, S. Zhang, L. Zhang, Z. Wu, W. Huang, S. Zeng, P. Hu, Understanding complete oxidation of methane on spinel oxides at a molecular level, *Nat. Commun.* 6 (2015) 7798, <https://doi.org/10.1038/ncomms7898>.
- [28] D.E. Jiang, S. Dai, The role of low-coordinate oxygen on Co₃O₄(110) in catalytic CO oxidation, *Phys. Chem. Chem. Phys.* 13 (2011) 978–984, <https://doi.org/10.1039/C0CP01138J>.
- [29] D. Pletcher, X. Li, S.W.T. Price, A.E. Russell, T. Sonmez, S.J. Thompson, Comparison of the spinels Co₃O₄ and NiCo₂O₄ as bifunctional oxygen catalysts in alkaline media, *Electrochim. Acta* 188 (2016) 286–293, <https://doi.org/10.1016/j.electacta.2015.10.020>.
- [30] S. Wang, B.Y. Guan, X.W. Lou, Rationally designed hierarchical N-doped carbon@NiCo₂O₄ double-shelled nanoboxes for enhanced visible light CO₂ reduction, *Energy Environ. Sci.* 11 (2018) 306–310, <https://doi.org/10.1039/C7EE02934A>.
- [31] Q. Huang, W. Li, Q. Lin, X. Zheng, H. Pan, D. Pi, C. Shao, C. Hu, H. Zhang, Catalytic performance of Pd-NiCo₂O₄/SiO₂ in lean methane combustion at low temperature, *J. Energy Inst.* 91 (2018) 733–742, <https://doi.org/10.1016/j.joei.2017.05.008>.
- [32] L. Wang, S. Zhang, Y. Zhu, A. Patlolla, J. Shan, H. Yoshida, S. Takeda, A.I. Frenkel, F. Tao, Catalysis and in situ studies of Rh₁/Co₃O₄ nanorods in reduction of NO with H₂, *ACS Catal.* 3 (2013) 1011–1019, <https://doi.org/10.1021/cs300816u>.
- [33] T. Bu, M. Wen, H. Zou, J. Wu, P. Zhou, W. Li, Z. Ku, Y. Peng, Q. Li, F. Huang, Y. Cheng, J. Zhong, Humidity controlled sol-gel Zr/TiO₂ with optimized band alignment for efficient planar perovskite solar cells, *Sol. Energy* 139 (2016) 290–296, <https://doi.org/10.1016/j.solener.2016.10.003>.
- [34] Y. Wang, Y. Li, Z. Lu, W. Wang, Improvement of O₂ adsorption for α-MnO₂ as an oxygen reduction catalyst by Zr⁴⁺ doping, *RSC Adv.* 8 (2018) 2963–2970, <https://doi.org/10.1039/C7RA10079E>.
- [35] J. Kim, D. Lee, J. Kim, S. Yang, J. Lee, Effects of H₂/O₂ mixed gas plasma treatment on electrical and optical property of indium tin oxide, *Appl. Surf. Sci.* 265 (2013) 145–148, <https://doi.org/10.1016/j.apsusc.2012.10.153>.
- [36] K.L. Purvis, G. Lu, J. Schwartz, S. Bernasek, Surface characterization and modification of indium tin oxide in ultrahigh vacuum, *J. Am. Chem. Soc.* 122 (2000) 1808–1809, <https://doi.org/10.1021/ja992910q>.
- [37] C. Zhang, L. Qi, Q. Chen, L. Lv, Y. Ning, Y. Hu, Y. Hou, F. Teng, Plasma treatment of ITO cathode to fabricate free electron selective layer in inverted polymer solar cells, *J. Mater. Chem. C* 2 (2014) 8715–8722, <https://doi.org/10.1039/C4TC0177C>.
- [38] T. Li, J. He, B. Pena, C.P. Berlinguet, Curing BiVO₄ photoanodes with ultraviolet light enhances photoelectrocatalysis, *Angew. Chem. Int. Ed.* 55 (2016) 1769–1772, <https://doi.org/10.1002/anie.201509567>.
- [39] M. Huang, Y. Zhang, F. Li, Z. Wang, N. Hu, Z. Wen, Q. Liu, Merging of Kirkendall growth and ostwald ripening: CuO@MnO₂ core-shell architectures for asymmetric supercapacitors, *Sci. Rep.* 4 (2014) 4518, <https://doi.org/10.1038/srep04518>.
- [40] J.Y. Kim, N. Choi, H.J. Park, J. Kim, D. Lee, H. Song, A hollow assembly and its three-dimensional network formation of single-crystalline Co₃O₄ nanoparticles for ultrasensitive formaldehyde gas sensors, *J. Phys. Chem. C* 118 (2014) 25994–26002, <https://doi.org/10.1021/jp505791v>.
- [41] F.A. Carey, *McGraw-Hill Higher Education*, (2000) Chapter 13.
- [42] Biological Magnetic Resonance Data Bank, The Board of Regents of the University of Wisconsin System.
- [43] C. Hammond, M.M. Forde, M.H. Ab Rahim, A. Thetford, Q. He, R.L. Jenkins, N. Dimitratos, J.A. Lopez-Sanchez, N.F. Dummer, D.M. Murphy, A.F. Carley, S.H. Taylor, D.J. Wilcock, E.E. Stangland, J. Kang, H. Hagen, C.J. Kiely, G.J. Hutchings, Direct catalytic conversion of methane to methanol in an aqueous medium by using copper-promoted Fe-ZSM-5, *Angew. Chem. Int. Ed.* 51 (2012) 5129–5133, <https://doi.org/10.1002/anie.201108706>.
- [44] T. Li, S.J. Wang, C.S. Yu, Y.C. Ma, K.L. Li, L.W. Lin, Direct conversion of methane to methanol over nano-[Au/SiO₂] in [Bmim]Cl ionic liquid, *Appl. Catal. A-Gen.* 398 (2011) 150–154, <https://doi.org/10.1016/j.apcata.2011.03.028>.
- [45] Q. Zhu, S.L. Wegener, C. Xie, O. Uche, M. Neurock, T.J. Marks, Sulfur as a selective ‘soft’ oxidant for catalytic methane conversion probed by experiment and theory, *Nat. Chem.* 5 (2013) 104–109, <https://doi.org/10.1038/NCHEM.1527>.
- [46] G. Pantaleo, V.L. Parola, F. Deganello, R.K. Singha, R. Bal, A.M. Venezia, Ni/CeO₂ catalysts for methane partial oxidation: synthesis driven structural and catalytic effects, *Appl. Catal. B-Environ.* 189 (2016) 233–241, <https://doi.org/10.1016/j.apcatb.2016.02.064>.
- [47] T. Ito, J.H. Lunsford, Synthesis of ethylene and ethane by partial oxidation of methane over lithium-doped magnesium oxide, *Nature* 314 (1985) 721–722, <https://doi.org/10.1038/314721b0>.
- [48] S.F. Ji, T.C. Xiao, S.B. Li, C.Z. Xu, R.L. Hou, K.S. Coleman, M.L.H. Green, The relationship between the structure and the performance of Na-W-Mn/SiO₂ catalysts for the oxidative coupling of methane, *Appl. Catal. A-Gen.* 225 (2002) 271–284, [https://doi.org/10.1016/S0926-860X\(01\)00864-X](https://doi.org/10.1016/S0926-860X(01)00864-X).
- [49] J. Shan, M. Li, L.F. Allard, S. Lee, M. Flytzani-Stephanopoulos, Mild oxidation of methane to methanol or acetic acid on supported isolated rhodium catalysts, *Nature* 551 (2017) 605–608, <https://doi.org/10.1038/nature24640>.
- [50] Y. Zhou, L. Zhang, W. Wang, Direct functionalization of methane into ethanol over

- copper modified polymeric carbon nitride via photocatalysis, *Nat. Commun.* 10 (2019) 506, <https://doi.org/10.1038/s41467-019-08454-0>.
- [51] L. Yu, Y. Shao, D. Li, Direct combination of hydrogen evolution from water and methane conversion in a photocatalytic system over Pt/TiO₂, *Appl. Catal. B-Environ.* 204 (2017) 216–223, <https://doi.org/10.1016/j.apcatb.2016.11.039>.
- [52] K. Villa, S. Murcia-Lopez, T. Andreu, J.R. Morante, Mesoporous WO₃ photocatalyst for the partial oxidation of methane to methanol using electron scavengers, *Appl. Catal. B-Environ.* 163 (2015) 150–155, <https://doi.org/10.1016/j.apcatb.2014.07.055>.
- [53] K. Villa, S. Murcia-Lopez, J.R. Morante, T. Andreu, An insight on the role of La in mesoporous WO₃ for the photocatalytic conversion of methane into methanol, *Appl. Catal. B-Environ.* 187 (2016) 30–36, <https://doi.org/10.1016/j.apcatb.2016.01.032>.
- [54] X. Yu, V.D. Waele, A. Lofberg, V. Ordomsky, A.Y. Khodakov, Selective photo-catalytic conversion of methane into carbon monoxide over zinc-heteropolyacid-titania nanocomposites, *Nat. Commun.* 10 (2019) 700, <https://doi.org/10.1038/s41467-019-08525-2>.
- [55] I. Bar-Nahum, A.M. Khenkin, R. Neumann, Mild, aqueous, aerobic, catalytic oxidation of methane to methanol and acetaldehyde catalyzed by a supported bipyridimidinylplatinum-polyoxometalate hybrid compound, *J. Am. Chem. Soc.* 126 (2004) 10236–10237, <https://doi.org/10.1021/ja0493547>.
- [56] Iwasita, Electrocatalysis of methanol oxidation, *Electrochim. Acta* 47 (2002) 3663–3674, [https://doi.org/10.1016/S0013-4686\(02\)00336-5](https://doi.org/10.1016/S0013-4686(02)00336-5).